First evidence for silica condensation within the solar protoplanetary disk

Mutsumi Komatsu[a,b,1], Timothy J. Fagan[b], Alexander N. Krot[c], Kazuhide Nagashima[c], Michail I. Petaev[d,e], Makoto Kimura[f,g], and Akira Yamaguchi[f,h]

[a]The Graduate University for Advanced Studies (SOKENDAI), Hayama, 240-0193 Kanagawa, Japan; [b]Department of Earth Sciences, Waseda University, Shinjuku, 169-8050 Tokyo, Japan; [c]Hawai'i Institute of Geophysics and Planetology, School of Ocean, Earth Science and Technology, University of Hawai'i at Mānoa, Honolulu, HI 96822; [d]Department of Earth and Planetary Sciences, Harvard University, Cambridge, MA 02138; [e]Harvard–Smithsonian Center for Astrophysics, Cambridge, MA 02138; [f]National Institute of Polar Research, Tachikawa, 190-8518 Tokyo, Japan; [g]Ibaraki University, 310-8512 Mito, Japan; and [h]Department of Polar Science, School of Multidisciplinary Science, SOKENDAI, Tachikawa, 190-8518 Tokyo, Japan

Edited by Mark H. Thiemens, University of California, San Diego, La Jolla, CA, and approved June 12, 2018 (received for review December 21, 2017)

Calcium-aluminum–rich inclusions (CAIs) and amoeboid olivine aggregates (AOAs), a refractory component of chondritic meteorites, formed in a high-temperature region of the protoplanetary disk characterized by approximately solar chemical and oxygen isotopic ($\Delta^{17}O \sim -24‰$) compositions, most likely near the protosun. Here we describe a ^{16}O-rich ($\Delta^{17}O \sim -22 \pm 2‰$) AOA from the carbonaceous Renazzo-type (CR) chondrite Yamato-793261 containing both (*i*) an ultrarefractory CAI and (*ii*) forsterite, low-Ca pyroxene, and silica, indicating formation by gas–solid reactions over a wide temperature range from ∼1,800 to ∼1,150 K. This AOA provides direct evidence for gas–solid condensation of silica in a CAI/AOA-forming region. In a gas of solar composition, the Mg/Si ratio exceeds 1, and, therefore, silica is not predicted to condense under equilibrium conditions, suggesting that the AOA formed in a parcel of gas with fractionated Mg/Si ratio, most likely due to condensation of forsterite grains. Thermodynamic modeling suggests that silica formed by condensation of nebular gas depleted by ∼10× in H and He that cooled at 50 K/hour at total pressure of 10^{-4} bar. Condensation of silica from a hot, chemically fractionated gas could explain the origin of silica identified from infrared spectroscopy of remote protostellar disks.

protoplanetary disk | refractory inclusions | meteorites

Chondritic meteorites (chondrites) are cosmic sedimentary rocks composed of three main components—refractory inclusions, chondrules, and fine-grained matrix—that formed largely in the protoplanetary disk and accreted into chondritic asteroids (1). Among the chondritic components, refractory inclusions are the oldest solar system solids dated (2) and, therefore, provide unique information about disk processes at the earliest stages of solar system evolution (3, 4). Based on textures and mineralogy, refractory inclusions are subdivided into Ca-Al–rich inclusions (CAIs) and amoeboid olivine aggregates (AOAs) (5). CAIs consist of minerals thermodynamically stable in a gas of solar composition at or above the condensation temperature of ferromagnesian olivine (forsterite, Mg_2SiO_4) (∼1,370 K at total pressure of 10^{-4} bar) and are thought to have formed by evaporation, condensation, and aggregation processes. Subsequently, some CAIs experienced melting followed by gas–melt–solid interactions. AOAs are aggregates rich in equant grains of forsterite with variable proportions of embedded CAIs; AOAs avoided significant melting after aggregation and, therefore, have retained records of gas–solid interactions (6–9). AOAs and unmelted CAIs from primitive (unmetamorphosed) chondrites have oxygen isotopic compositions enriched in ^{16}O relative to the terrestrial oxygen fractionation line [i.e., $\Delta^{17}O \sim -24‰$, where $\Delta^{17}O = \delta^{17}O - 0.52 \times \delta^{18}O$, $\delta^{i}O = (({}^{i}O/{}^{16}O)_{sample}/({}^{i}O/{}^{16}O)_{SMOW} - 1) \times 1{,}000$, i = 17 or 18, and SMOW is Standard Mean Ocean Water] (10–12). This ^{16}O-enriched composition is similar to that of the solar wind ($\Delta^{17}O = -28 \pm 2‰$) returned by the NASA Genesis mission (13). Multiple settings of formation and thermal processing of refractory inclusions may have existed in the solar nebula (e.g., ref. 14). However, based on the high formation temperatures and the ^{16}O-rich compositions characteristic of refractory inclusions, it is likely that CAIs and AOAs formed in an isotopically distinct region close to the protosun (1).

Most AOAs from unmetamorphosed or weakly metamorphosed chondrites contain fine-grained high-Ca pyroxene, anorthite, and ±spinel surrounded by nearly pure forsterite and ±Fe,Ni-metal, indicating preservation of early-stage, high-temperature Ca,Al-rich condensates followed by condensation of forsterite and ±Fe,Ni-metal at somewhat lower temperatures (15). Variations in Mn/Fe ratios observed in low-iron, Mn-enriched olivines in some AOAs may reflect a range of olivine condensation temperatures (7, 8, 16). In the peripheral portions of ∼10% of AOAs studied, forsterite is corroded by low-Ca pyroxene ($MgSiO_3$), indicative of continuous interaction between forsterite and gaseous SiO as ambient temperature decreased to ∼1,300 K (17, 18).

Here we describe an AOA (AOA 4) with evidence of formation over an unusually wide temperature range from the carbonaceous Renazzo-type (CR) chondrite Yamato-793261 (Y-793261). To characterize AOA 4 and its host meteorite, we used optical microscopy, secondary electron microscopy (SEM), electron probe microanalyses (EPMA), Raman spectroscopy, and secondary ion mass spectrometry (SIMS); the GRAINS thermodynamic/kinetic

Significance

The oldest solar system solids dated are refractory inclusions [Ca-Al–rich inclusions (CAIs) and amoeboid olivine aggregates (AOAs)], which occur in chondritic meteorites and provide records of high-temperature processes in the early solar system. An ultrarefractory CAI and the silica-phase quartz occur in an AOA from the carbonaceous chondrite Yamato-793261, indicating formation over a temperature range exceeding 650 K. The minerals have ^{16}O-rich compositions consistent with the nebular setting associated with refractory inclusions. This AOA provides direct evidence that silica condensed from gas in a CAI/AOA-forming region in our solar system indicates that gas became Si-rich as Mg condensed and may explain the origin of silica detected from infrared spectroscopy of T Tauri and asymptotic giant branch stars.

Author contributions: M. Komatsu designed research; M. Komatsu, A.N.K., K.N., M.I.P., M. Kimura, and A.Y. performed research; M. Komatsu, T.J.F., A.N.K., K.N., M.I.P., M. Kimura, and A.Y. analyzed data; and M. Komatsu, T.J.F., A.N.K., K.N., M.I.P., M. Kimura, and A.Y. wrote the paper.

The authors declare no conflict of interest.

This article is a PNAS Direct Submission.

[1]To whom correspondence should be addressed. Email: komatsu_mutsumi@soken.ac.jp.

This article contains supporting information online at www.pnas.org/lookup/suppl/doi:10.1073/pnas.1722265115/-/DCSupplemental.

Published online July 2, 2018.

code for condensation was then used to model formation conditions of AOA 4 (for details, see *SI Appendix*, *Analytical Methods*).

Petrology of AOA 4 in CR Chondrite Y-793261

The Y-793261 meteorite is composed of chondrules, refractory inclusions, mineral fragments, and fine-grained matrix. It experienced a minor degree of aqueous alteration that resulted in partial replacement of chondrule glass and matrix by phyllosilicates and of Fe,Ni-metal by magnetite and Fe,Ni-sulfides; olivine and pyroxene phenocrysts in chondrules, however, are largely unaltered. Similar alteration features are described in weakly altered CR chondrites of petrologic types 2.5–2.6 (19).

Raman spectra were collected on randomly selected matrix areas in a polished thin section of Y-793261. It has been shown previously that D and G bands (at ~1,350 and ~1,600 cm^{-1}, respectively) in Raman spectra of organic matter in chondrite matrices vary with thermal metamorphic recrystallization of the host meteorite. Namely, the full width, half-maximum (FWHM) of the D band decreases and the intensity ratio I_D/I_G increases with thermal maturity of the organic matter (20–22). For comparison with Y-793261, Raman spectra were also collected from matrix areas in thin sections of Allan Hills (ALH) 77307 [carbonaceous Ornans-type (CO) 3.03], Y-81020 (CO 3.05), Efremovka [carbonaceous Vigarano-type (CV) 3.1–3.4], Axtell (CV > 3.6), Allende (CV > 3.6) (petrologic subtypes from refs. 21 and 23), and eight CR chondrites of the National Institute of Polar Research (NIPR) collection.

The wide FWHM-D and low I_D/I_G of Y-793261 indicate that this meteorite experienced only weak thermal metamorphism (Fig. 1). The Raman parameters are similar to other CRs that we analyzed (labeled CRs-NIPR in Fig. 1). Busemann et al. (24) and Quirico et al. (25) collected Raman spectra from diverse chondrites, including CRs. The Quirico et al. (25) data are similar to our results for I_D/I_G but have slightly lower FWHM-D; the Busemann et al. (24) data for CRs overlap with ours but range to higher I_D/I_G and lower FWHM-D. Differences between the three datasets are not surprising given that (*i*) they are based on different CR meteorites and (*ii*) spectra reported by refs. 24 and 25 were collected from extracted insoluble organic matter and raw matrix grains, respectively, whereas our data were collected from matrix areas of polished thin sections. Nonetheless, the low thermal maturity of organic matter indicated by Raman spectra (refs. 24 and 25 and this study) shows that most CR chondrites, including Y-793261, as well as CM (carbonaceous Mighei-type) chondrites, did not undergo thermal metamorphism to the same extent as most type 3 ordinary, CO (Ornans-type), and CV (Vigarano-type) chondrites (26) (Fig. 1). Some CR and CM chondrites have relatively low FWHM-D and high I_D/I_G, probably due to shock heating (refs. 25 and 27 and this study; CRs and CMs-heated in Fig. 1); however, these meteorites are relatively rare. Thus, the Raman data confirm the supposition that most CRs have a high probability of preserving minerals and textures of nebular origin (26, 28–31).

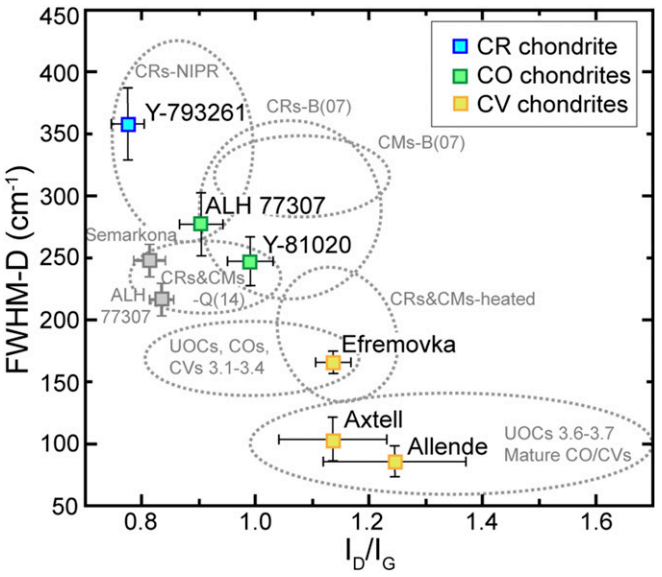

Fig. 1. Spectral parameters of Raman bands of carbonaceous matter from matrix of Y-793261 compared with other carbonaceous and type 3 ordinary chondrites. Analyses shown in colored squares were conducted at NIPR (*SI Appendix, Analytical Methods*); error bars show ±1σ uncertainty based on ~20 analyses per sample. Analyses shown in gray are from ref. 20 (for Semarkona) and ref. 22 (for ALH 77307). Fields outlined in gray summarize data from (*i*) seven NIPR Antarctic CR chondrites (CRs-NIPR, analyses collected at NIPR during this study); (*ii*) insoluble organic matter (IOM) grains extracted from CR chondrites and CM chondrites analyzed by ref. 24, labeled CRs-B(07) and CMs-B(07), respectively; (*iii*) matrix grains of CR and CM chondrites [ref. 25, labeled CRs&CMs-Q(14)]; (*iv*) heated CR and CM chondrites (refs. 25 and 27 and this study, labeled CRs&CMs-heated); and (*v*) unequilibrated ordinary chondrites (UOCs), CVs, and COs of petrologic types 3.1–3.4, vs. types ≥3.6 (20–22).

AOA 4 consists of an aggregate of nearly pure forsterite (Fo_{97-99}) and low-Ca pyroxene enclosing multiple fine-grained Ca-Al–rich minerals, including Al,Ti-diopside (in wt %, 5–10 Al_2O_3, 2–4 TiO_2; *SI Appendix*, Table S1), anorthite, and ±spinel (Fig. 2 *A*–*C*). Olivine occurs as a circuitous chain of equant grains no more than 10 μm across. Low-Ca pyroxene forms thin (1–2 μm across) layers around some olivine crystals and also occurs in 5- to 10-μm–sized aggregates of individual grains. Fe-hydroxide–rich veins cutting the AOA are probably due to terrestrial weathering in Antarctica.

Silica is present at a few localities in the AOA interior, where it occurs as anhedral, ~5-μm–sized grains associated with low-Ca pyroxene (Fig. 2 *A* and *D*). Raman spectra of the silica grains show a sharp peak at 464 cm^{-1}, diagnostic of quartz (Fig. 2*E*). The quartz in AOA 4 is similar in texture to the more refractory AOA minerals (interlocking textures typical of igneous crystallization and vein quartz typical of an alteration origin are conspicuously absent) suggesting an origin by gas–solid reactions, although the original SiO_2 phase might have been a phase other than quartz. At 1 bar pressure, transitions to higher-temperature silica polymorphs, tridymite and crystobalite, occur at ~1,150 and ~1,740 K, respectively (32, 33).

One of the Ca-Al–rich domains of AOA 4 is mineralogically distinct: it consists of Zr,Sc,Al,Ti-rich pyroxenes (in wt %, 20–32 Al_2O_3, 5–15 TiO_2, and 2–8 Sc_2O_3 and ZrO_2; *SI Appendix*, Table S1), compositionally similar to davisite (34), enclosing submicron grains of Zr-rich oxides and spinel, and surrounded by Al,Ti-diopside (Fig. 2 *F* and *G*). Zirconium and scandium (Sc) are very refractory elements, with 50% condensation temperatures at 10^{-4} bar of 1,764 K for Zr and 1,659 K for Sc (35). In several previous studies, temperature-fractionated rare earth element (REE) patterns have been used as criteria for characterizing a given CAI as ultrarefractory (UR) (e.g., refs. 36–39), but REE concentrations have not been determined yet for the UR CAI in AOA 4. Nonetheless, Zr,Sc-rich pyroxene and/or oxides are characteristic minerals of previously identified UR CAIs and, in light of the high condensation temperatures of Zr and Sc, are indicators of crystallization at UR conditions (40, 41).

Concentrations of ZrO_2 and Sc_2O_3 in pyroxene are highest in the core of the Ca-Al–rich domain and decrease toward its peripheral boundary with typical AOA forsterite. This zoning may be roughly analogous to normal zoning in igneous systems in that an early-stage, high-temperature composition was preserved in a crystal that grew while temperature declined. The positive correlation between ZrO_2 and Sc_2O_3 at or above the solar value is similar to pyroxenes in UR CAIs 3N-24 from CV3 chondrite northwest Africa (NWA) 3118 and 33E-1 from the CV3 Efremovka (40) (Fig. 3). Fassaitic pyroxenes in UR CAIs Murchison HIB-11 and Efremovka 101.1 also have positive correlations between ZrO_2 and Sc_2O_3 but at subsolar Zr/Sc, possibly as a

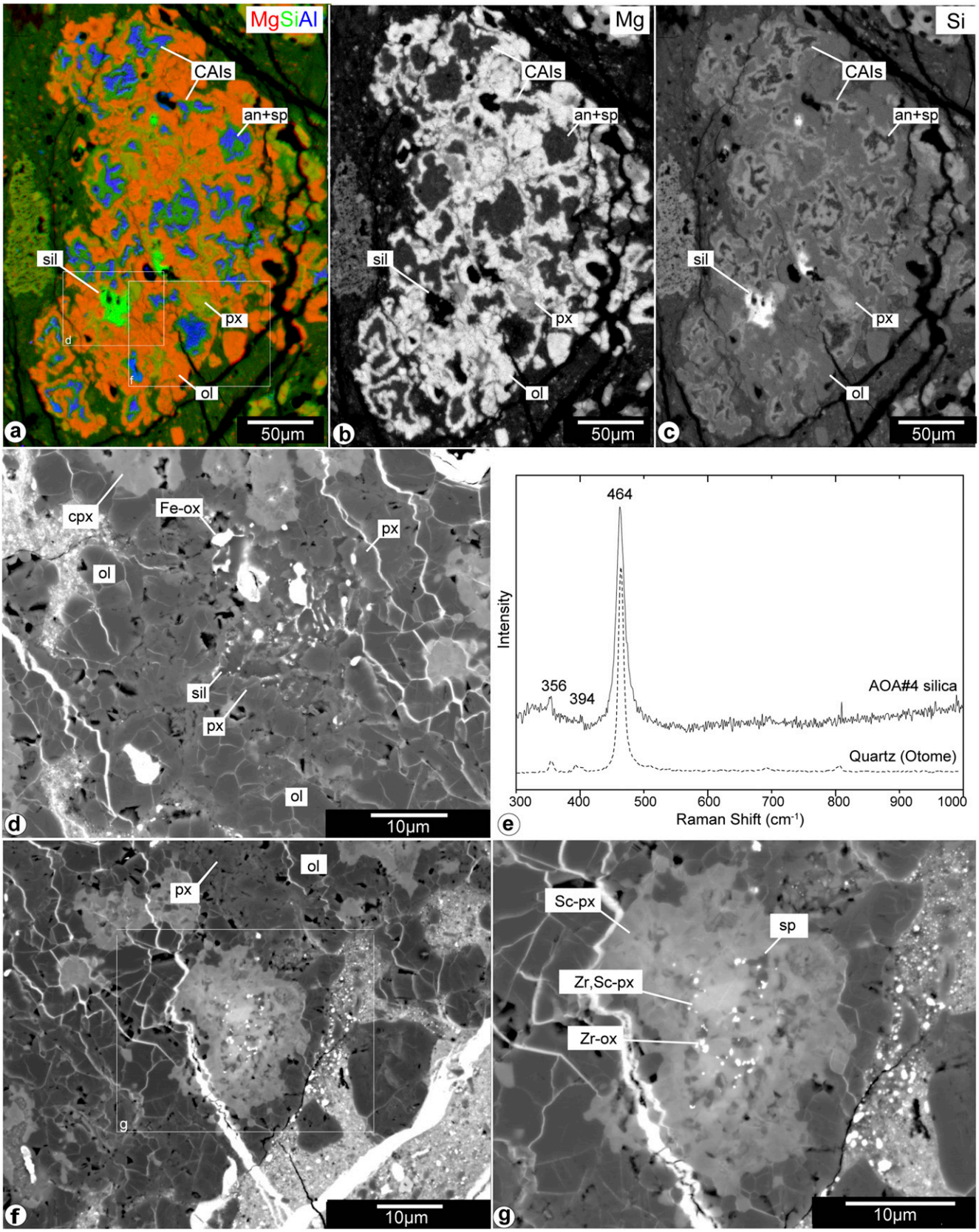

Fig. 2. (*A*) Combined elemental map of AOA 4 in Y-793261 in Mg (red), Si (green), and Al Kα (blue) X-rays. Elemental maps in (*B*) Mg and (*C*) Si. (*D*) BSE image of silica-bearing part of AOA 4. (*E*) Raman spectra of silica grains, showing a sharp peak at 464 cm^{-1}, diagnostic of quartz, with quartz from Otome mine, Yamanashi prefecture, Japan, for comparison. (*F* and *G*) BSE images of UR CAI embedded in Y-793261 AOA 4. Regions outlined in *A* and *F* are shown in detail in *D*, *F*, and *G*. Abbreviations are as follows: an, anorthite; CAIs, Ca,Al-rich inclusions; cpx, Al,Ti-diopside; Fe-ox, iron hydroxide; ol, olivine; px, low-Ca pyroxene; Sc-px, Sc-rich pyroxene; sil, quartz; sp, spinel; and Zr,Sc-px, Zr,Sc-rich pyroxene.

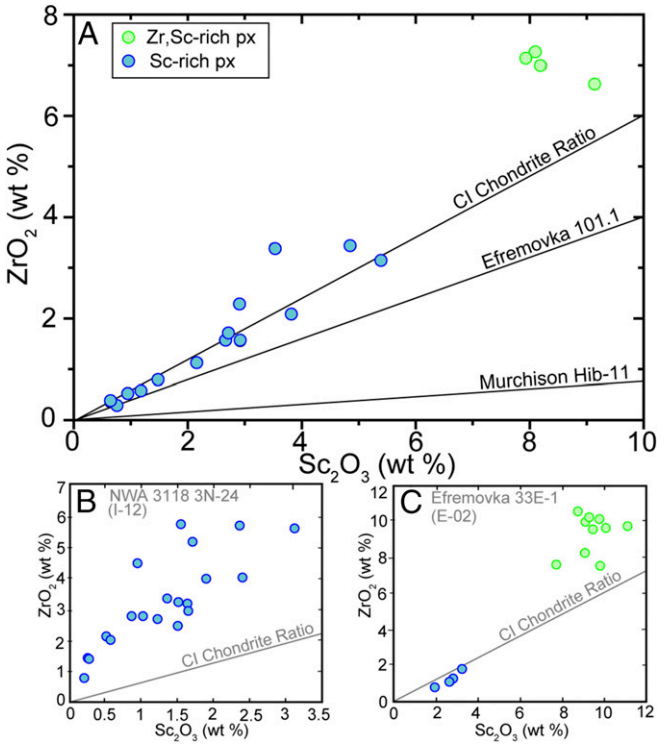

Fig. 3. (*A*) Comparison of ZrO_2/Sc_2O_3 ratios in Zr,Sc-bearing pyroxenes from the UR CAI in Y-793261 AOA 4 with those of UR CAIs Murchison Hib-11 (37) and Efremovka 101.1 (38) and (*B* and *C*) ratios from UR CAIs NWA 3118 3N-24 and Efremovka 33E-1 (40).

consequence of partitioning between phases during post-condensation partial melting (37, 38) (Fig. 3). In the UR CAI-like domain of AOA 4 and in CAI 33E-1, the most Zr,Sc-rich pyroxene compositions have Zr/Sc ratios above the solar value, which may reflect temperature-dependent fractionation of the more refractory Zr. Chondritic Zr/Sc ratios of the less Zr,Sc-rich pyroxene suggest that melting did not occur after original crystallization. The presence of UR minerals indicates that initial formation of AOA 4 either (*i*) started at higher temperatures than other AOAs in CR chondrites or (*ii*) started at temperatures similar to other AOAs but cooled so rapidly that early-formed UR minerals did not reequilibrate at lower temperatures.

Oxygen Isotope Compositions of Minerals in AOA 4

Forsterite, Al-diopside, low-Ca pyroxene, quartz, and Zr,Sc-rich pyroxenes in AOA 4 have similar ^{16}O-rich compositions ($\Delta^{17}O \sim -22 \pm 2‰$; *SI Appendix*, Table S2 and Fig. 4) typical of CAIs and AOAs from unmetamorphosed chondrites (e.g., refs. 10–12). The uniformly ^{16}O-rich composition of the AOA is distinctly different from the ^{16}O-poor compositions of whole-rock samples of CR chondrites (ref. 42 and references therein) (Fig. 4*A*), olivine and pyroxene phenocrysts in CR chondrules ($\Delta^{17}O \sim -6$–$0‰$) (e.g., ref. 43), and secondary carbonates and magnetite that precipitated from aqueous solutions in CR matrices ($\Delta^{17}O \sim -3$ to $+2‰$) (44). These observations indicate that the minerals in AOA 4 originated in an ^{16}O-rich gaseous setting of approximately solar composition and subsequently avoided oxygen isotopic exchange with ^{16}O-poor reservoirs, such as nebular gas associated with chondrule formation and aqueous fluid associated with alteration of CR chondrites (1, 10, 43).

The presence of ultrarefractory Zr- and Sc-rich pyroxene, spinel, anorthite, Al-diopside, low-Ca pyroxene, and quartz within a single AOA provides evidence for a large temperature range during gas–solid reactions recorded by this object, between ~1,800 and ~1,150 K. Given the high condensation temperatures of Zr and Sc (36), the ultrarefractory CAI could have formed by either evaporation or condensation at ~1,700–1,800 K. The less refractory spinel-anorthite-Al-diopside CAIs recorded gas–solid interaction at much lower temperature: the 50% condensation temperatures of these minerals are ~1,400–1,350 K. Forsterite condensed directly from the nebular gas at 1,375 K:

$$2Mg_{(g)} + SiO_{(g)} + 3H_2O_{(g)} = Mg_2SiO_{4(s)} + 3H_{2(g)}. \quad \textbf{[R1]}$$

Low-Ca pyroxene becomes stable at ~1,300 K (45). Two textural occurrences of low-Ca pyroxene in AOA 4 (rims around forsterite grains and aggregates of euhedral crystals) may indicate its formation by two mechanisms: by interaction between forsterite and gaseous SiO,

$$Mg_2SiO_{4(s)} + SiO_{(g)} + H_2O_{(g)} = 2MgSiO_{3(s)} + H_{2(g)}, \quad \textbf{[R2]}$$

and by direct gas–solid condensation,

$$Mg_{(g)} + SiO_{(g)} + H_2O_{(g)} = MgSiO_{3(s)} + H_{2(g)}. \quad \textbf{[R3]}$$

The ^{16}O-rich low-Ca pyroxenes replacing forsterites (Reaction **R2**) have been previously described in ~10% of AOAs from

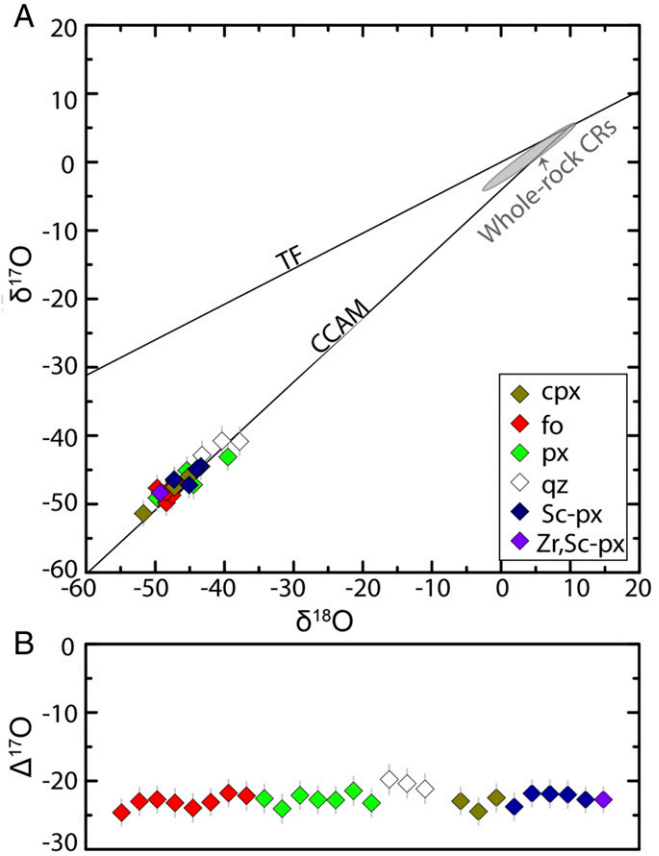

Fig. 4. (*A*) Three-oxygen isotope ($\delta^{17}O$ vs. $\delta^{18}O$) diagram and (*B*) $\Delta^{17}O$ values of individual minerals from the Y-793261 AOA 4. Field showing compositions of whole-rock CR chondrites (from ref. 42 and references therein) is shown for comparison. All minerals in the AOA plot near the carbonaceous chondrite anhydrous mineral (CCAM) line and have ^{16}O-rich compositions ranging from −20 to −25‰ in $\Delta^{17}O$. cpx, Al,Ti-diopside; fo, forsterite; px, low-Ca pyroxene; qz, quartz; Sc-px, Sc-rich pyroxene; Zr,Sc-px, Zr,Sc-rich pyroxene. The TF line is shown for reference.

carbonaceous chondrites (17, 18). The direct gas–solid condensation of ^{16}O-rich low-Ca pyroxenes (Reaction **R3**) has been proposed to explain ^{16}O-rich ($\Delta^{17}O \sim -24‰$) low-Ca pyroxenes grains dispersed in matrix of the K chondrite Kakangari (46).

Condensation Calculations

In a gas of solar composition, the Mg/Si ratio exceeds 1 (35), and silica is not predicted to condense under equilibrium conditions (e.g., refs. 3 and 47). The existence of silica in AOA 4 suggests that the parcel of gas in which it formed underwent extensive Mg/Si fractionation similar to the condensation with partial isolation model (45, 47). Here we used the GRAINS code (48) to explicitly model how variations in pressure, dust/gas ratio, and cooling rate affect the isolation of Mg and Si in growing forsterite grains, which, in turn, may affect the condensation sequence (45, 47). A specific feature that distinguishes the GRAINS code (*Materials and Methods*) from other condensation codes is that it calculates the amount of condensate isolated in the cores of metal and olivine grains based on their sizes which, in turn, depend upon number densities of corresponding atoms in the gas (defined by the gas composition and pressure) and cooling rate. Therefore, the observed sizes of olivine grains in AOA 4 place an important constraint on pressure during condensation.

We modeled condensation of gas of solar composition and gas depleted in H_2 and He by a factor of 10 relative to the solar value in the pressure range of 10^{-3} to 10^{-6} bar assuming different cooling rates as summarized in *SI Appendix*, Table S3. The ferromagnesian minerals of AOA 4 contain sufficient FeO (all analyses ≥0.6 wt %; *SI Appendix*, Table S1) to imply condensation under more oxidizing conditions than those of the classic solar nebula (3, 47). Following ref. 47, we assume that more oxidizing conditions were caused by local depletion of the solar nebula in H_2 (and He) gas, which is expressed as dust to gas ratio (D/G). The admissible pressure range is found to be ∼10^{-3} to 10^{-5} bar. At higher pressures, condensation of forsterite is preceded by a significant amount of Fe,Ni-metal, which is inconsistent with our petrographic observations. At lower pressures, small sizes of forsterite grains, irrespective of cooling rate, result in nearly complete equilibration with the ambient gas so a silica polymorph never forms.

We find that the observed forsterite grain size (∼5 μm) and chemical composition of low-Ca pyroxene (*SI Appendix*, Table S1) are reasonably matched by condensation of nebular gas depleted by ∼10× in H_2 and He that cools at a constant rate of 50 K/h at a total pressure of 10^{-4} bar (*SI Appendix*, Table S3). Forsterite grains start to grow by condensation from the gas at 1,525 K and reach ∼5 μm across at 1,440 K when they start to react with gaseous SiO to form low-Ca pyroxene. At 1,435 K forsterite grains become completely isolated from the gas, whereas the low-Ca pyroxene continues to condense alone until cocondensation of cristobalite begins at 1,417 K. Quartz becomes stable below 1,169 K; it would form by either transformation of cristobalite or thermal annealing of amorphous silica if the latter condensed instead of cristobalite, which is likely at such rapid cooling. The estimated cooling rate of AOA 4, similar to that of igneous CAIs (5), implies a rapid (hours) processing of AOAs and CAIs in the early solar nebula, perhaps, on highly localized scales (47) and slightly variable dust-to-gas ratios.

Astrophysical Implications

The presence of silica condensates in dust shells of oxygen-rich asymptotic giant branch stars has been previously suggested from infrared spectroscopic observations (49). Presolar silica grains characterized by isotopically anomalous O isotope compositions were subsequently identified in matrices of chondrites ALH 77307 (CO3.03) (50) and of LaPaZ 031117 (CO3.0) and Grove Mountains 021710 (CR2) (51). Based on infrared spectra of T Tauri stars with the Spitzer Space Telescope, the presence of crystalline silica (tridymite or cristobalite) was also inferred in protoplanetary disks around T Tauri stars, where its origin was attributed to incongruent melting of enstatite to form a silica-enriched liquid, followed by rapid cooling, possibly during transient heating events hypothesized to create chondrules (52). An igneous origin of remotely detected silica is consistent with the presence of igneous tridymite and cristobalite in chondrules from primitive chondrites (53, 54) and in 81P/Wild 2 cometary dust returned by the NASA Stardust mission (55, 56).

AOA 4 from CR chondrite Y-793261 provides an alternative to an igneous origin of silica in protoplanetary disks and constitutes direct evidence for gas–solid condensation of ^{16}O-rich silica coincident with formation of refractory inclusions in the solar nebula. We conclude that the presence of UR minerals and silica in the same AOA in a CR chondrite resulted from a condensation with partial isolation-type process (45).

Materials and Methods

A polished thin section of Y-793261 was studied using SEM, EPMA, Raman spectroscopy, and SIMS oxygen isotopic analyses. Petrologic observations and mineral identifications were made using a JEOL JSM-7100F field emission scanning electron microscope (FE-SEM) with backscattered electron (BSE) mode at NIPR, Japan. Semiquantitative compositional analyses for fine-grained minerals and X-ray elemental mapping were also performed with an energy dispersive spectroscopic detector (Oxford AZtek system) attached to the JSM-7100F FE-SEM, with a 3-nA electron beam accelerated at a voltage of 15 kV. Quantitative elemental analyses were performed using a JEOL JXA-8200 electron microprobe at NIPR. Analyses were conducted at 15 kV and a sample current of 20 nA olivine and 30 nA for Ca-rich pyroxene. For the Ca-rich pyroxene analyses that contain Sc and Zr, pulse height analyzer settings were adjusted to minimize X-ray interferences of Sc Kα and Zr Lα.

Raman spectra were collected from polished thin sections using a JASCO NRS-1000 Raman microspectrometer at NIPR using 532-nm excitation. For each analysis, the laser light was focused to a spot size of 2–3 μm using a 40× microscope objective. Spectra were acquired under atmospheric conditions in the spectral region 1,000–1,800 cm^{-1} for matrix and 300–1,000 cm^{-1} for silica.

Oxygen isotope compositions were measured in situ using the University of Hawai'i (UH) Cameca ims-1280 secondary ion mass spectrometer. A primary Cs^+ ion beam accelerated to 10 keV was used to sputter the sample with an impact energy of 20 keV. Due to small grain sizes in the AOA (<10 μm in diameter), an ∼20-pA primary beam focused to ∼1–2 μm was used. A normal incident electron flood gun was used for charge compensation with homogeneous electron density over a region of ∼70 μm in diameter. Three oxygen isotopes were measured simultaneously using a Faraday cup detector for $^{16}O^-$ and two electron multipliers for $^{17}O^-$ and $^{18}O^-$. Mass resolving power (M/ΔM, 10% definition) on ^{16}O and ^{18}O was set to ∼2,000, whereas ^{17}O was measured with a mass resolving power of ∼5,500, which is sufficient to almost completely resolve the interfering $^{16}OH^-$ from the $^{17}O^-$. Because of the abundance sensitivity tail of the $^{16}OH^-$ peak, we made a small tail correction (typically <0.1‰) on $^{17}O^-$ based on $^{16}OH^-$ count rate measured after each measurement. Data were collected for 30 cycles of 20 s each.

For accurate locations of SIMS analyses, we used the UH JEOL 5900LV SEM to focus the electron beam on spots we intended to measure. Exposing the electron beam to the surface for 5–20 min leaves a submicrometer hole in the carbon coat, which can be recognized as a mark on the spot of interest from a $^{16}O^-$ scanning ion image in the ion probe, as described by ref. 46. Oxygen isotope compositions are reported as $\delta^{17}O$ and $\delta^{18}O$, deviations from SMOW in parts per thousand,

$$\delta^{17,18}O_{SMOW} = \left[\left(^{17,18}O/^{16}O_{sample}\right)/\left(^{17,18}O/^{16}O_{SMOW}\right)-1\right]\times 1000,$$

and as $\Delta^{17}O$, deviation from the terrestrial fractionation (TF) line,

$$\Delta^{17}O = \delta^{17}O - 0.52\times\delta^{18}O.$$

The reported 2σ uncertainties include both the internal measurement precision on an individual analysis and the external reproducibility of standard measurements during a given analytical session.

The GRAINS thermodynamic and kinetic code calculates equilibrium partitioning of 33 elements among 242 gaseous and 520 condensed species (48). It contains two subroutines which model growth of Fe,Ni-metal and olivine grains by condensation based on kinetic theory of condensation and subsequent diffusional redistribution of elements along grain radii in response to changing temperature and surface concentrations of the elements as the gas–dust assemblage of the solar nebula cools. For given temperature, pressure,

and system composition the GRAINS code first calculates equilibrium mole fractions of condensed and gaseous species, then sizes of metal and olivine grains and their compositional profiles, then outputs abundances and chemical compositions of stable phases and zoning profiles of metal and olivine, adjusts mass balance by subtracting the amounts of isolated elements, changes the temperature by a specified increment, and repeats the cycle.

See *SI Appendix* for more details on analytical techniques and modeling.

ACKNOWLEDGMENTS. We thank the National Institute of Polar Research, Japan, for supplying meteorite thin sections. We also thank three anonymous reviewers and Editor Natasha V. Raikhel for helpful comments and insightful suggestions. This work was supported by JSPS KAKENHI Grant 16K05603 (to M. Komatsu, PI), NASA Emerging Worlds program, Grant NNX15AH38G (to A.N.K., PI), NASA Emerging Worlds program, Grant NNX15AH44H (to K.N., PI), MEXT KAKENHI Grant 26400510 (to M. Kimura, PI), NIPR Project Research KP307, General Collaboration Project No. 26-30 (to M. Kimura, A.Y.).

1. Scott ERD, Krot AN (2014) Chondrites and their components. *Meteorites and Cosmochemical Processes*, ed Davis AM, Treatise on Geochemistry, Vol 1, eds Holland HD, Turekian KK (Elsevier, Oxford), pp 65–137.
2. Connelly JN, et al. (2012) The absolute chronology and thermal processing of solids in the solar protoplanetary disk. *Science* 338:651–655.
3. Ebel DS (2006) Condensation of rocky material in astrophysical environments. *Meteorites and the Early Solar System II*, eds Lauretta DS, McSween, Jr HY (University of Arizona Press, Tucson, AZ), pp 253–277.
4. Krot AN, et al. (2009) Origin and chronology of chondritic components: A review. *Geochim Cosmochim Acta* 73:4963–4998.
5. MacPherson GJ (2014) Calcium-aluminum-rich inclusions in chondritic meteorites. *Meteorites, Comets and Planets: Treatise on Geochemistry*, eds Davis AM, Holland HD, Turekian KK, (Elsevier, Oxford), Vol 1, pp 139–179.
6. Komatsu M, et al. (2001) Mineralogy and petrography of amoeboid olivine aggregates from the reduced CV3 chondrites Efremovka, Leoville and Vigarano: Products of nebular condensation, accretion and annealing. *Meteorit Planet Sci* 36:629–641.
7. Komatsu M, Fagan TJ, Mikouchi T, Petaev MI, Zolensky ME (2015) LIME silicates in amoeboid olivine aggregates in carbonaceous chondrites: Indicator of nebular and asteroidal processes. *Meteorit Planet Sci* 50:1271–1294.
8. Weisberg MK, Connolly HC, Jr, Ebel DS (2004) Petrology and origin of amoeboid olivine aggregates in CR chondrites. *Meteorit Planet Sci* 39:1741–1753.
9. Sugiura N, Petaev MI, Kimura M, Miyazaki A, Hiyagon H (2009) Nebular history of amoeboid olivine aggregates. *Meteorit Planet Sci* 44:559–572.
10. Yurimoto H, et al. (2008) Oxygen isotopes of chondritic components. *Rev Mineral Geochem* 68:141–186.
11. Makide K, et al. (2009) Oxygen- and magnesium-isotope compositions of calcium-aluminum-rich inclusions from CR2 carbonaceous chondrites. *Geochim Cosmochim Acta* 73:5018–5051.
12. Krot AN, Park C, Nagashima K (2014) Amoeboid olivine aggregates from CH carbonaceous chondrites. *Geochim Cosmochim Acta* 139:131–153.
13. McKeegan KD, et al. (2011) The oxygen isotopic composition of the Sun inferred from captured solar wind. *Science* 332:1528–1532.
14. Kawasaki N, Simon SB, Grossman L, Sakamoto N, Yurimoto H (2018) Crystal growth and disequilibrium distribution of oxygen isotopes in an igneous Ca-Al-rich inclusion from the Allende carbonaceous chondrite. *Geochim Cosmochim Acta* 221:318–341.
15. Krot AN, et al. (2004) Amoeboid olivine aggregates and related objects in carbonaceous chondrites: Records of nebular and asteroid processes. *Chem Erde* 64:185–239.
16. Ebel DS, Weisberg MK, Beckett JR (2012) Chemical stability of low-iron, manganese-enriched olivine in astrophysical environments. *Meteorit Planet Sci* 47:585–593.
17. Krot AN, Petaev MI, Yurimoto H (2004) Amoeboid olivine aggregates with low-Ca pyroxenes: A genetic link between refractory inclusions and chondrules? *Geochim Cosmochim Acta* 68:1923–1941.
18. Krot AN, Fagan TJ, Nagashima K, Petaev MI, Yurimoto H (2005) Origin of low-Ca pyroxene in amoeboid olivine aggregates: Evidence from oxygen isotopic compositions. *Geochim Cosmochim Acta* 69:1873–1881.
19. Harju ER, et al. (2014) Progressive aqueous alteration of CR carbonaceous chondrites. *Geochim Cosmochim Acta* 139:267–292.
20. Quirico E, Raynal P-I, Bourot-Denise M (2003) Metamorphic grade of organic matter in six unequilibrated ordinary chondrites. *Meteorit Planet Sci* 38:795–881.
21. Bonal L, Quirico E, Bourot-Denise M, Montagnac G (2006) Determination of the petrologic type of CV3 chondrites by Raman spectroscopy of included organic matter. *Geochim Cosmochim Acta* 70:1849–1863.
22. Bonal L, Bourot-Denise M, Quirico E, Montagnac G, Lewin E (2007) Organic matter and metamorphic history of CO chondrites. *Geochim Cosmochim Acta* 71:1605–1623.
23. Kimura M, Grossman JN, Weisberg MK (2008) Fe-Ni metal in primitive chondrites: Indicators of classification and metamorphic conditions for ordinary and CO chondrites. *Meteorit Planet Sci* 43:1161–1177.
24. Busemann H, Alexander CMO'D, Nittler LR (2007) Characterization of insoluble organic matter in primitive meteorites by microRaman spectroscopy. *Meteorit Planet Sci* 42:1387–1416.
25. Quirico E, et al. (2014) Origin of insoluble organic matter in type 1 and 2 chondrites: New clues, new questions. *Geochim Cosmochim Acta* 136:89–99.
26. Bonal L, et al. (2013) Hydrogen isotopic composition of the water in CR chondrites. *Geochim Cosmochim Acta* 106:111–133.
27. Briani G, et al. (2013) Short duration thermal metamorphism in CR chondrites. *Geochim Cosmochim Acta* 122:267–279.
28. Krot AN, Meibom A, Weisberg MK, Keil K (2002) The CR chondrite clan: Implications for early solar system processes. *Meteorit Planet Sci* 37:1451–1490.
29. Abreu NM, Brearley AJ (2010) Early solar system processes recorded in the matrices of two highly pristine CR3 carbonaceous chondrites, MET 00426 and QUE 99177. *Geochim Cosmochim Acta* 74:1146–1171.
30. Alexander CMO'D, Howard KT, Bowden R, Fogel ML (2013) The classification of CM and CR chondrites using bulk H, C and N abundances and isotopic compositions. *Geochim Cosmochim Acta* 123:244–260.
31. Davidson J, et al. (2014) Abundances of presolar silicon carbide grains in primitive meteorites determined by NanoSIMS. *Geochim Cosmochim Acta* 139:248–266.
32. Holmquist SB (1961) Conversion of quartz to tridymite. *J Am Ceram Soc* 44:82–86.
33. Presnall DC (1995) Phase diagrams of Earth-forming minerals. *Mineral Physics and Crystallography. A Handbook of Physical Constants*, ed Ahrens TJ (American Geophysical Union, Washington, DC), pp 248–268.
34. Ma C, Rossman GR (2009) Davisite, $CaScAlSiO_6$, a new pyroxene from the Allende meteorite. *Am Mineral* 94:845–848.
35. Lodders K (2003) Solar system abundances and condensation temperatures of the elements. *Astrophys J* 591:1220–1247.
36. Davis AM (1991) Ultrarefractory inclusions and the nature of the group II REE fractionation. *Meteoritics* 26:330.
37. Simon SB, Davis AM, Grossman L (1996) A unique ultrarefractory inclusion from the Murchison meteorite. *Meteorit Planet Sci* 31:106–115.
38. El Goresy A, et al. (2002) Efremovka 101.1: A CAI with ultrarefractory REE patterns and enormous enrichments of Sc, Zr, and Y in fassaite and perovskite. *Geochim Cosmochim Acta* 66:1459–1491.
39. Hiyagon H, Hashimoto A, Kimura M, Ushikubo T (2003) First discovery of an ultrarefractory nodule in an Allende fine grained inclusion. *34th Lunar and Planetary Science Conference, March 17–21, League City, TX* (Lunar and Planetary Institute, Houston).
40. Ivanova MA, Krot AN, Nagashima K, MacPherson GJ (2012) Compound ultrarefractory CAI-bearing inclusions from CV3 carbonaceous chondrites. *Meteorit Planet Sci* 47: 2107–2127.
41. Zhang A-C, et al. (2015) Mineralogical anatomy and implications of a Ti-Sc-rich ultrarefractory inclusion from Sayh al Uhaymir 290 CH3 chondrite. *Geochim Cosmochim Acta* 163:27–39.
42. Schrader DL, et al. (2011) The formation and alteration of the Renazzo-like carbonaceous chondrites I: Implications of bulk-oxygen isotopic composition. *Geochim Cosmochim Acta* 75:308–325.
43. Schrader DL, et al. (2013) The formation and alteration of the Renazzo-like carbonaceous chondrites II: Linking O-isotope composition and oxidation state of chondrule olivine. *Geochim Cosmochim Acta* 101:302–327.
44. Jilly-Rehak CE, Huss GR, Nagashima K, Schrader DL (2018) Low-temperature aqueous alteration on the CR chondrite parent body: Implications from *in situ* oxygen-isotope analyses. *Geochim Cosmochim Acta* 222:230–252.
45. Petaev MI, Wood J (1998) The condensation with partial isolation (CWPI) model of condensation in the solar nebula. *Meteorit Planet Sci* 33:1123–1137.
46. Nagashima K, Krot AN, Huss GR (2015) Oxygen-isotope compositions of chondrule silicates and matrix grains in Kakangari K-grouplet chondrite. *Geochim Cosmochim Acta* 151:49–67.
47. Petaev MI, Wood J (2005) Meteoritic constraints on temperatures, pressures, cooling rates, and modes of condensation in the solar nebula. *Chondrites and the Protoplanetary Disk*. Astronomical Society of the Pacific Conference Series, eds Krot AN, Scott ERD, Reipurth B (Astronomical Society of the Pacific, San Francisco), Vol 341, pp 373–406.
48. Petaev MI (2009) The GRAINS thermodynamic and kinetic code for modeling nebular condensation. *Calphad* 33:317–327.
49. Speck AK, Barlow MJ, Sylvester RJ, Hofmeister AM (2000) Dust features in the 10-μm infrared spectra of oxygen-rich evolved stars. *Astron Astrophys Suppl Ser* 146: 437–464.
50. Bose M, Floss C, Stadermann FJ, Stroud RM, Speck AK (2012) Circumstellar and interstellar material in the CO3 chondrite ALHA77307: An isotopic and elemental investigation. *Geochim Cosmochim Acta* 93:77–101.
51. Haenecour P, Zhao X, Floss C, Lin Y, Zinner E (2013) First laboratory observation of silica grains from core collapse supernovae. *Astrophys J Lett* 768:L17.
52. Sargent BA, et al. (2009) Silica in protoplanetary disks. *Astrophys J* 690:1193–1207.
53. Krot AN, Libourel G, Goodrich CA, Petaev MI (2004) Silica-rich igneous rims around magnesian chondrules in CR carbonaceous chondrites: Evidence for fractional condensation during chondrule formation. *Meteorit Planet Sci* 39:1931–1955.
54. Kimura M, et al. (2005) Thermal history of the enstatite chondrites from silica polymorphs. *Meteorit Planet Sci* 40:855–868.
55. Zolensky ME, et al. (2006) Mineralogy and petrology of comet 81P/Wild 2 nucleus samples. *Science* 314:1735–1739.
56. Mikouchi T, et al. (2007) Mineralogy and crystallography of Comet 81P/Wild 2 particles. *38th Lunar and Planetary Science Conference, March 12–16, 2007, League City, TX* (Lunar and Planetary Institute, Houston), p 1946.